Cobalt Phosphate Nanostructures for Non-Enzymatic Glucose Sensing at Physiological pH

Pietro Pacchin Tomanin,[†] Pavel V. Cherepanov,[†,⊥] Quinn A. Besford,[†] Andrew J. Christofferson,[‡] Alessia Amodio,[#] Chris F. McConville,[§] Irene Yarovsky,[‡] Frank Caruso,[,†] and Francesca Cavalieri[*†,#]*

[†]ARC Centre of Excellence in Convergent Bio-Nano Science and Technology, and the Department of Chemical Engineering, The University of Melbourne, Parkville, Victoria 3010, Australia

[‡]School of Engineering, RMIT University, GPO Box 2476, Melbourne, Victoria 3001, Australia

[#] Department of Chemical Science and Technologies, University of Rome Tor Vergata, via della ricerca scientifica 1, 00133 Rome, Italy

[§]College of Science, Engineering and Health, RMIT University, GPO Box 2476, Melbourne, Victoria 3001, Australia

KEYWORDS: Cobalt phosphate, nanoflowers, density functional theory, non-enzymatic, glucose sensing.

ABSTRACT

Nanostructured materials have great potential as platforms for analytical assays and catalytic reactions. Herein, we report the synthesis of electrocatalytically active cobalt phosphate nanostructures (CPNs) using a simple, low-cost, and scalable preparation method. The electrocatalytic properties of the CPNs toward the electrooxidation of glucose (Glu) were studied by cyclic voltammetry and chronoamperometry in relevant biological electrolytes, such as phosphate-buffered saline (PBS), at physiological pH (7.4). Using the CPNs, Glu detection could be achieved over a wide range of biologically relevant concentrations, from 1 to 30 mM Glu in PBS, with a sensitivity of 7.90 nA/mM cm^2 and a limit of detection of 0.3 mM, thus fulfilling the necessary requirements for human blood Glu detection. In addition, the CPNs showed a high structural and functional stability over time at physiological pH. The CPN-coated electrodes could also be used for Glu detection in the presence of interfering agents (e.g., ascorbic acid and dopamine) and in human serum. Density functional theory calculations were performed to evaluate the interaction of Glu with different faceted cobalt phosphate surfaces; the results revealed that specific surface presentations of under-coordinated cobalt led to the strongest interaction with Glu, suggesting that enhanced detection of Glu by the CPNs can be achieved by lowering the surface coordination of cobalt. Our results highlight the potential use of phosphate-based nanostructures as catalysts for electrochemical sensing of biochemical analytes.

INTRODUCTION

Nanostructured materials with highly accessible surface areas and exposed facets have proven useful in applications spanning catalysis,[1] sensing,[2] and energy storage.[3] These materials are typically fabricated using inorganic nanoparticles,[4] nanowires,[5] and nanosheets,[6] which allows the surface structure and functionality of the resulting materials to be tailored.[7] However, harsh conditions are typically employed for the synthesis, involving multiple steps, toxic reagents, and extremes in pH and temperature. The development of new synthetic strategies for engineering nanostructured surfaces under mild conditions, and with enhanced catalytic properties, is therefore desirable.

Recently, the synthesis of hybrid organic–inorganic nanostructured materials, such as nanoflowers, was reported under moderate synthetic conditions.[8] Briefly, a metal salt (e.g., composed of copper, calcium, or manganese ions) is dissolved in phosphate-buffered saline (PBS) in the presence of macromolecules. The functional groups of the macromolecules provide sites for the nucleation and subsequent growth of metal phosphate crystals, leading to the formation of nanostructured phosphate-based microparticles with a high surface-to-volume ratio. These highly structured materials have primarily been used for the immobilization of enzymes that ultimately achieve superior enzymatic performances.[8-11] Similar phosphate-based materials have also been synthesized, however, in the absence of organic motifs, that is without macromolecules.[12,13] Materials that display accessible surface areas,[14] high index facets,[15] and sharp edges,[16] and are composed of transition metals,[17-19] are potentially useful in the field of electrocatalysis for sensing biochemical analytes.[20] Notably,

materials containing electroactive cobalt metal ions based on phosphates,[13] phosphides,[20] nitrites[21] and oxides[18] have recently shown promise for their use in electrochemical applications such as water splitting,[22] energy storage,[13] and sensing.[23]

Particularly, the development of accurate, inexpensive, and stable glucose (Glu) detection devices is an expanding field where the key goal is to reduce costs associated with the measurements, ultimately leading to increased patient compliance for patients diagnosed with metabolic diseases such as diabetes. A variety of methods have been developed for Glu sensing and include processes based on enzymatic reactions,[24-26] Glu-specific conjugation chemistry,[27] supramolecular recognition,[28] and direct electrochemical oxidation.[29,30] Commercial methods used for blood Glu level detection involve enzymatic sensors. However, these enzymatic sensors have drawbacks in terms of material cost,[31] measurement variability with temperature, pH, humidity, and interfering chemical species, and enzyme stability.[32] These disadvantages have thus generated interest in developing non-enzymatic Glu sensors. Examples of non-enzymatic systems developed to date are based on noble metals,[33,34] alloys,[35] transition metals,[21,36] and hybrid organic–inorganic structures comprising carbon nanotubes[37] and graphene.[38] However, despite these recent developments, several problems remain to be addressed relative to the high cost of the component materials, the complexity of the fabrication method, the specificity of the sensor to the analyte, and the limit and range of detection. Importantly, the poor performance of existing sensors in detecting Glu at near biological conditions, such as in an aqueous buffer at physiological pH, has limited the use of non-enzymatic Glu sensing systems in real-life applications.[23,39-43]

Herein, we develop a low-cost and scalable one-pot approach to fabricate electrocatalytically active cobalt phosphate nanostructures (CPNs) under mild synthetic conditions. The CPNs are amorphous, exhibit high surface areas, and can catalyze the electrooxidation of Glu in aqueous buffer at physiological pH. Upon coating an electrode with the CPNs, the electrooxidation of Glu can be quantified as a function of Glu concentration—the CPN-coated electrode can achieve a wide range of detection between 1 and 30 mM Glu in aqueous buffer (PBS), with a sensitivity of 7.90 nA/mM cm^2 at 5mM of Glu based on electroactive surface area (ESA) and a limit of detection (LOD) of 0.3 mM (signal-to-noise ratio (S/N) = 3). In addition, the CPN-coated electrode exhibits high stability with time and can detect Glu in the presence of common interfering agents (ascorbic acid and dopamine) and in human serum (HS). Density functional theory (DFT) calculations were performed to investigate the interaction between Glu and the surface of the CPN sensor. The results show that the interaction of the CPNs with Glu is due to the presentation of under-coordinated cobalt atoms at the interface of the CPN material. Our results highlight the potential use of the CPNs for the electrochemical detection of biochemical analytes.

EXPERIMENTAL METHODS

Reagents and Chemicals. Cobalt(II) nitrate hexahydrate ($Co(NO_3)_2{\cdot}6H_2O$, ≥97%, CAS no. 10026-22-9) was purchased from Baker. PBS tablets, Nafion® 117 (CAS no. 31175-20-9), cobalt(II) phosphate hydrate ($Co_3(PO_4)_2{\cdot}xH_2O$, CAS no. 10294-50-5), potassium ferricyanide(III) ($K_3Fe(CN)_6$, CAS no. 13746-66-2), and HS from human male AB plasma were purchased from Sigma-Aldrich. D-Glucose (CAS no. 50-99-7) was purchased from AnalR.

Potassium chloride (KCl, CAS no. 7440-09-7) was purchased from Chem-Supply. All the chemicals were used as received. High purity (Milli-Q) water with a resistivity of 18.2 MΩ cm was obtained from an inline Millipore RiOs/Origin water purification system.

Instrumentation. X-ray photoelectron spectroscopy (XPS) spectra were acquired using an Axis Ultra X-ray photoelectron spectrometer (Kratos Analytical, UK), equipped with a 165 mm concentric hemispherical electron energy analyzer and a monochromated Al Kα incident X-ray source (1486.6 eV). Survey (wide) scans were recorded in the binding energy range of 0–1200 eV, with 1.0 eV steps, a dwell time of 100 ms, and an analyzer pass energy of 160 eV. Multiplex (narrow) high-resolution spectra were recorded with a pass energy of 20 eV, with 0.05 eV steps, and a dwell time of 250 ms, resulting in an energy resolution ($\Delta E/E$) of ~300 meV. The base pressure in the analysis chamber during data collection was $1–2 \times 10^{-9}$ mbar, and these data were processed using the software CasaXPS. All binding energies were calibrated using the C 1s level of adventitious carbon at 285.0 eV. Fourier transform infrared (FTIR) spectra were obtained on a Tensor II (Bruker) attenuated total reflectance Fourier transform infrared (ATR-FTIR) spectrometer and analyzed using the software OPUS 7.8. The number of scans was 64. A minimum resolution of 4 cm^{-1} and the absorbance/transmittance mode were used. Scanning electron microscopy (SEM) images were obtained on a Teneo VolumeScope (FEI) microscope. Transmission electron microscopy (TEM) was conducted on a Tecnai Spirit (FEI) microscope operating at 120 kV. Energy-dispersive X-ray spectroscopy (EDX) was performed on a 20 mm^2 X-Max SDD instrument (Oxford Instruments) equipped with the software AZtec 3.2. X-ray diffraction (XRD) data were collected using a D8 Advance

X-ray diffractometer (Bruker) with Ni-filtered Cu kα radiation (1.54 Å). Data were collected between 5 and 85° 2θ, with a step size of 0.02° and a scan rate of 1.0 s per step. An anti-scatter blade was used to reduce the diffracted background intensity at low angles. An incident beam divergence of 1.0° was used with a 2.5° soller slit in the diffracted beam. The sample was spun at 15 revolutions per minute. Generally, unless otherwise specified, the data from the characterizations were exported to the software OriginPro 8.5 for further analysis.

Synthesis of Cobalt Phosphate Nanostructures. An aqueous $Co(NO_3)_2{\cdot}6H_2O$ solution (100 μL, 1.2 M) was added to PBS (20 mL, 1 mM, pH 7.4) in a 50 mL tube with simultaneous vortexing, which was continued for 5 s after addition, followed by static aging at 23 °C overnight. For the scale-up of the synthesis, an aqueous $Co(NO_3)_2{\cdot}6H_2O$ solution (10 mL, 1.2 M) was added to PBS (2 L, 1 mM, pH 7.4) in a 2 L glass beaker with vigorous stirring, which was continued for 5 s after addition, followed by static aging at 23 °C overnight. The precipitate was then collected, washed 5 times by centrifugation (67 *g*, 5 min) and resuspension in water, and finally resuspended in water (40 mL) and stored at 4 °C for further characterizations. SEM and TEM samples were prepared by drop casting the aqueous suspension on a silicon wafer and a carbon grid, respectively, followed by drying in air. XPS, XRD, and FTIR samples were prepared by drying the aqueous suspension in a vacuum desiccator prior to analysis.

Electrode Preparation. A glassy carbon electrode (GCE, 3 mm in diameter) was first polished with a 0.05 μm alumina slurry. The polished GCE was then rinsed with water and ethanol, and allowed to dry in air. A CPN suspension (10 mg/mL) in 10% (v/v) Nafion in ethanol was prepared and vortexed to obtain a homogeneous suspension. On the center of the GCE, the

prepared suspension (10 μL) was drop cast and allowed to dry in air. Similarly, a screen-printed electrode (SPE, 3 mm in diameter) was modified by drop casting a 10 mg/mL CPN suspension (10 μL) in 10% (v/v) Nafion in water and allowed to dry in air. A total mass of 0.1 mg of CPNs was deposited on the GCE or SPE to achieve complete surface coverage of the working electrode. A bare GCE electrode for control measurements was prepared following the aforementioned procedure without the use of CPNs, thereby resulting in an electrode coated with Nafion only. For comparison, GCE was also modified with $Co_3(PO_4)_2$ powder following the aforementioned protocol. Graphite SPE chips that were produced from the Laboratory of Biosensors & Nanomachines at the University of Rome, Tor Vergata were used. Briefly, the electrodes were printed using a 245 DEK (Weymouth, UK) screen-printing machine and graphite-based (Loctite edag PF-407A) and silver-based (Loctite edag PF-410) conductive inks and a grey dielectric paste insulating ink. The inks were printed on a polyester flexible film (Autostat HT5). Each graphite SPE chip contained three separate printed portions that served as the working (carbon-based ink), the reference (silver-based ink), and the counter electrode (carbon-based ink). The diameter of the working electrode was 3 mm, which resulted in an apparent geometric area of 7.07 mm^2.

Electrochemical Measurements. Cyclic voltammetry (CV) and chronoamperometry (CA) measurements were performed on a MM510 potentiostat/galvanostat (Materials Mates Italia S.r.l.) using the software VoltaScope 5.4. Electrochemical measurements involving the GCE were conducted in a three-electrode electrochemical cell composed of a glassy carbon working electrode (3 mm diameter), a platinum wire as the counter electrode, and a Ag/AgCl reference

electrode. Electrochemical measurements involving the screen-printed electrode, SPE, were performed on the screen-printed electrode described above. The supporting electrolyte, unless specified otherwise, was a N_2-saturated 10 mM PBS solution (pH 7.4) that was thoroughly mixed by a magnetic stirrer. The pH of the electrolyte was adjusted, when needed, with 1 M NaOH solution.

Computational Details. The X-ray crystal structure[44] of $Co_3(PO_4)_2$ was obtained based on the most likely cobalt phosphate stoichiometry determined from the XRD pattern of the CPNs and cleaved to form the (100), (111), and (211) surfaces. For the (111) and (211) surfaces, oxygen positions were adjusted to preserve the tetrahedral phosphate geometry. Each slab consisted of two layers, with $x \times y$ dimensions of 16.72 × 8.79, 9.77 × 12.13, and 17.47 × 12.13 Å^2 for the (100), (111), and (211) surfaces, respectively. Increasing the number of layers or replicating the unit cell in the x or y dimension did not affect the Glu binding energies significantly. A vacuum spacer of at least 20 Å in the z-direction was added, and the model surfaces were subsequently relaxed, generating surface structures corresponding to different possibilities of surface cobalt coordination. Following surface relaxation, the geometry of the bottom layer of the slabs was frozen for the surface–Glu binding energy calculations. For the free Glu structural optimization, a single Glu molecule was placed in the center of a 20 × 20 × 20 Å^3 box, and only the gamma point was sampled. For the adsorption calculations, a variety of initial orientations of Glu on the relaxed surfaces were constructed, with an O1(Glu)–cobalt initial distance of ~2.5 Å. All calculations were performed using the Vienna *Ab Initio* Simulation Package (VASP)[45] and the generalized gradient approximation (GGA) Perdew–Burke–Ernzerhof

(PBE)[46] exchange correlation functional. The projector augmented wave (PAW) method[47] was used with the Blöchl all-electron, frozen-core PAW pseudopotentials.[48] A $5 \times 5 \times 1$ Monkhorst-Pack[49] k-point mesh for sampling the Brillouin zone and a cutoff energy of 500 eV were applied, and spin polarization was included. A dipole correction was applied to minimize polarization effects due to slab asymmetry. The Hubbard U parameter (GGA + U)[50] for the electron correlation of the d states in cobalt ions was used with a value of 3.5 eV.[51] A convergence criterion of 0.01 eV/Å was employed for the geometry optimizations.

RESULT AND DISCUSSION

Preparation and Characterization of CPNs. The CPNs were synthesized using a one-pot crystallization method in water at neutral pH and at 23 °C. Briefly, $Co(NO_3)_2 \cdot 6H_2O$ solution was added to PBS with mixing for 5 s. The resulting solution was then allowed to age statically overnight (Figure 1a). After ca. 30 min following the addition of $Co(NO_3)_2 \cdot 6H_2O$, the solution turned from a transparent pale red to an opaque dispersion. After aging overnight, a dark purple precipitate had formed at the bottom of the flask leaving an almost transparent supernatant. These observations suggest that the Co^{2+} ions are involved in the formation of the solid precipitate. The morphology of the precipitate was characterized by SEM and TEM. The SEM images in Figure 1b,c reveal the open flower-like network of the CPNs. The flower-like structures were about 3 μm in diameter and were composed of smaller sub-unit nanosheets that had a thickness of about 20 nm and a width of about 100 nm. The TEM images in Figure 1d,e indicated that the distribution of the nanosheets was denser at the core than in the outer layer of the particles. The spatially organized length of the network spans from the nano- to

the microscale, providing both exposed facets and a high surface-to-volume ratio. In contrast, $Co_3(PO_4)_2$ powder is composed of aggregates of sheets with thickness and lateral dimensions of around 400 nm and 4 μm, respectively (Figure S1). These dimensions are significantly larger than the dimensions of the prepared CPNs.

The EDX and XPS analyses of the CPNs, shown in Figure 1f–i, reveal the presence of the elements Co, P, and O in the sample. In addition, EDX analysis indicates a bulk Co/P ratio of 1:0.4 (Figure S2), whereas the XPS analysis shows a surface Co/P ratio of 1:6 (Figure S3). The surface composition determined from XPS data of the Co and P 2p levels was accounted considering the sensitivity factors. Hence, we conclude that the composition of the CPNs is nonhomogeneous.

The XPS survey spectrum in Figure S3 shows the presence of a prominent O 1s peak and characteristic core-level peaks of Co and P. The Co 2p XPS spectra (Figure 1g) displayed Co $2p_{3/2}$ and Co $2p_{1/2}$ peaks, with each peak consisting of contributions from Co^{2+} and Co^{3+} respectively observed at 780.6 and 782.6 eV for the Co $2p_{3/2}$ peak and at 796.5 and 789.3 eV for the Co $2p_{1/2}$ peak. In addition, two broad satellite (Sat.) features were observed at 780.6 and 782.6 eV. The intensity of the satellite features appears to be enhanced indicating a contribution from the presence of $Co(OH)_2$ and phosphate species on the surface.[52] As shown in Figure 1h, two peaks, P $2p_{3/2}$ and P $2p_{1/2}$, were also present in the P 2p region at 132.3 and 133.2 eV, respectively. These peaks are consistent with the characteristic binding energies of tetrahedral (PO_4) groups.[53] The O 1s peak could be resolved into three components, with the main core-level oxygen line at 530.5 eV and two satellites at 532.0 and 533.0 eV. Although the

assignment of these satellites features is controversial in the literature, the peak at 533.0 eV could be attributed to OH species present in small quantities of cobalt hydroxide, whereas the peak at 532.0 eV could be assigned to the presence of a layer of loosely bound oxygen at the surface of the CPNs. As the core binding energies relative to Co 2p and O 1s of cobalt oxides and hydroxides are in the same range as those of cobalt phosphate, we suggest that the surface of the CPNs constitutes a combination of Co^{2+} and Co^{3+} as oxo/hydroxo and phosphate species, however, with the latter phosphate species believed to be more predominant in line with the Co/P ratio of 1:6 determined by XPS.[54]

The typical XRD pattern of the CPNs in Figure 1j indicates that the sample lacks crystalline features. The XRD pattern could be closely matched to the $Co_3(PO_4)_2 \cdot H_2O$ phase. The ATR-FTIR spectrum of the CPNs in Figure 1k displayed peaks at around 580 cm^{-1} and in the 3500–2500 and 1200–900 cm^{-1} regions. The broad absorption in the region from 3500 to 2500 cm^{-1} and the weak peak at 1607 cm^{-1} were assigned to the vibration of the OH groups, suggesting the presence of water of crystallization and hydroxyl groups within the structure.[55] The vibration frequencies present in the region from 1200 to 900 cm^{-1} are characteristic of phosphate groups.[56] The two overlapping intense peaks at 567 and 586 cm^{-1} are characteristic of the stretching vibrations of the metal–oxygen bond.[57] The morphological properties of the CPNs suggest the potential use of this material as electrocatalysts.

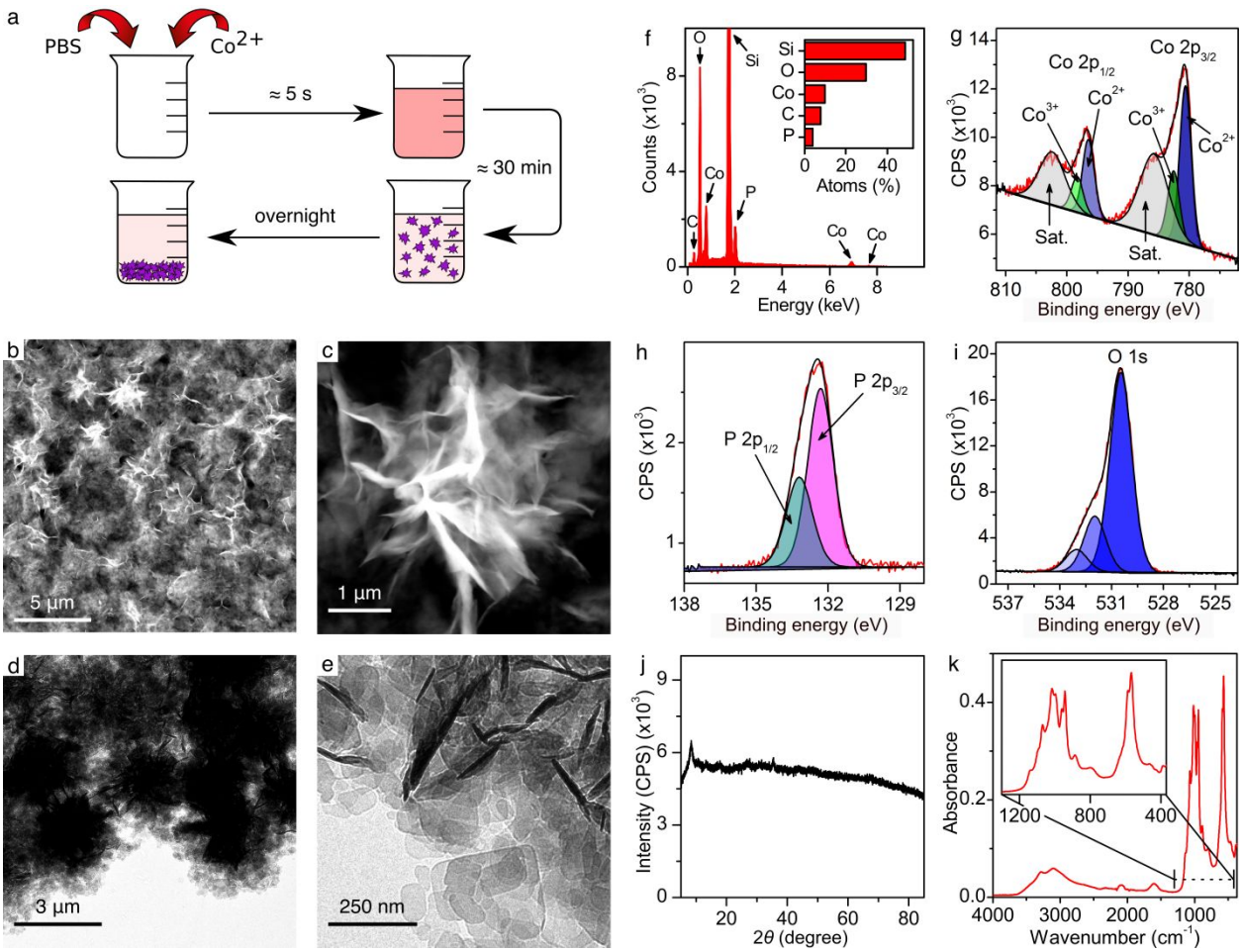

Figure 1. (a) Schematic illustration of the proposed mechanism for CPN formation. (b,c) SEM and (d,e) TEM images of the CPNs at various magnification. (f) EDX spectrum, (g,h,i) high-resolution Co 2p (g), P 2p (h), and O1s (i) XPS spectra, (j) XRD spectrum, and (k) ATR-FTIR spectrum of the CPNs (the inset in (k) shows a magnified portion of spectrum in the range of 1300–370 cm^{-1}).

Electrochemical Characterization of CPNs. A schematic illustration of the preparation of electrode surfaces with the CPNs and the setup used for the electrochemical studies is shown in Figure 2a. Briefly, a suspension of the CPNs was drop cast on the GCE and electrochemically

characterized using a three-electrode cell with PBS as the supporting electrolyte. A SPE that was prepared in a similar manner was used for the detection of Glu in HS. A SPE was selected because of its small size, as this would allow for low-volume measurements. In addition, the SPE device is portable and disposable. The drop casting technique, which is a common and widespread approach used for preparing electrodes, was selected as it allows for facile and fast deposition.

CV and CA experiments were conducted to characterize the electrochemical properties of the CPN electrode. Figure 2b shows the first 30 consecutive CV cycles of the CPNs obtained at a scan rate of 20 mV/s and in the potential range from –0.2 to 0.9 V. After the first few cycles, broad reduction and oxidation peaks were observed in the potential region of 0.35–0.65 V. These two peaks were respectively assigned to the oxidation and reduction of the Co ions. The inset in Figure 2b displays the oxidation current response of the CPNs at 0.65 V over the 30 CV cycles ran; a gradual increase in current was observed as the cycle number increased. This upward trend can potentially be explained by the migration of anions to the electrode surface, which counterbalance the electrostatic charge from the oxidized Co cations, and subsequently penetrate the CPNs with successive CV cycles, thereby generating and expanding percolation pathways within the catalyst leading to an increase of the electroactive surface area.[58] As the abovementioned process enhances the electrochemical response of the CPN, 30 CV cycles were run as an activation step.

Figure 2c displays the CV cycles of the CPN electrode in PBS at various scanning rates ranging from 20 to 60 mV/s. Faster scanning rates resulted in an increase in both the anodic

and cathodic peak currents, suggesting a limiting process in the Co^{3+}/Co^{4+} redox reaction. The inset in Figure 2c shows the linear relationship between the peak currents and the square root of the scan rate at neutral pH, indicating that the Co^{3+}/Co^{4+} redox reaction is a diffusion-controlled process.[59] The fitting values are reported in Table S1.

The effective surface area of the activated CPN-modified GCE was measured via CV at varying scan rates of 20–270 mV/s in a non-mixed 5 mM $K_3Fe(CN)_6$ and 0.1 M KCl supporting electrolyte by the ferri-/ferrocyanide redox couple method (Figure 2d).[60] The inset in Figure 2d shows the relationship between the peak current associated to the $Fe(CN)_6^{3-}/Fe(CN)_6^{4-}$ pair and the square root of the scan rate. This relationship can be described by Equation 1:

$$i_{peak} = 268600An^{3/2}D^{1/2}Cv^{1/2} \quad (1)$$

where i_{peak} (A) is the peak current, A (cm^2) is the effective surface area, n (1) is the number of electrons transferred in the process, D (7.3×10^{-6} cm^2/s) is the diffusion coefficient of $Fe(CN)_6^{3-}$ at 25 °C,[61] C (5×10^{-6} mol cm^{-3}) is the concentration of $Fe(CN)_6^{3-}$, and v (V/s) is the scan rate. The slope of the plot in the inset of Figure 2d was used to calculate the effective surface area A using Equation 1. The calculated effective surface area of the CPN-modified GCE was 46.63 cm^2, which is about 660 times larger than the geometrical area of the electrode ($\approx 7 \times 10^{-2}$ cm^2).

To elucidate the electrochemical properties of the CPNs, several CV cycles in PBS at different pHs at a scanning rate of 20 mV/s in the potential region from –0.2 to 0.9 V were performed (Figure S4). At pH 10.5, an overall increase in the magnitude of the current density

was observed with the most pronounced oxidation and reduction peaks observed at, respectively, 0.30 and 0.65, and 0.15 and 0.50 V. These peaks could be attributed to the reduction/oxidation of Co^{2+}/Co^{3+} and Co^{3+}/Co^{4+} redox couples, respectively.[23,36,62,63]

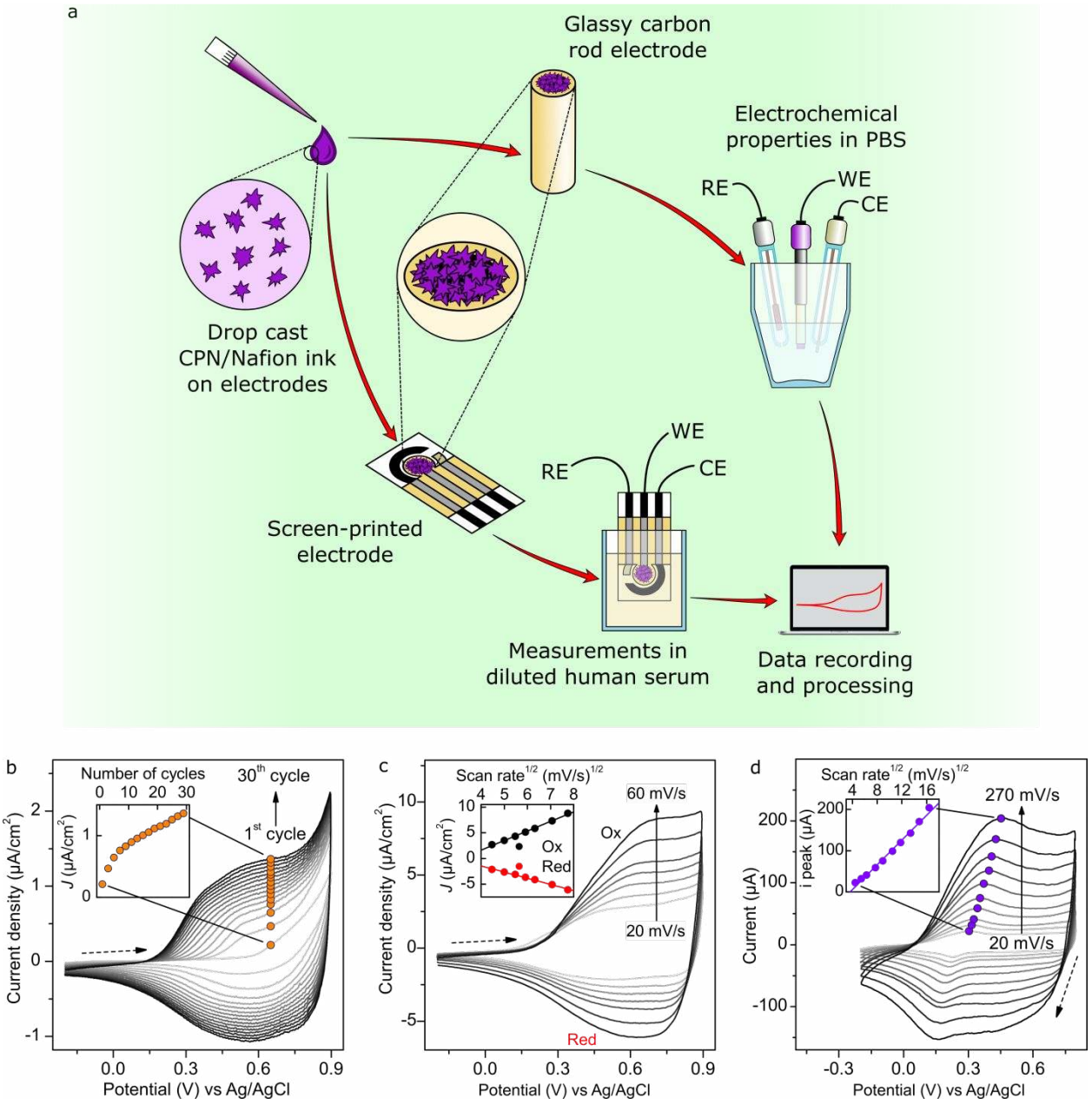

Figure 2. (a) Schematic representation of the preparation of the glassy carbon electrode and screen-printed electrode, the experimental setup used for the electrochemical characterizations, and measurements performed in the electrolyte composed of human serum and PBS. WE, working electrode; CE, counter electrode; RE, reference electrode. (b) CV cycles (30) of the CPNs in a N_2-saturated PBS electrolyte (10 mM, pH 7.4) at a scan rate of 20 mV/s. The inset shows a plot of the peak current density value at 0.65 V vs Ag/AgCl as a function of the cycle number. (c) CVs of the CPNs in PBS buffer (10 mM, pH 7.4) at different scan rates: 20, 25, 30, 35, 40, 50, and 60 mV/s. The inset shows a plot of the oxidation (Ox) and reduction (Red) peaks current densities as a function of the square root of the scan rate. (d) CVs of the CPNs in 5 mM $K_3Fe(CN)_6$/0.1 M KCl supporting electrolyte at different scan rates from 20 to 270 mV/s. The inset shows a plot of the peak current of the $Fe(CN)_6^{3-}/Fe(CN)_6^{4-}$ redox couple as a function of the square root of the scan rate. Dashed arrows indicate the potential sweep direction. All current density data are normalized by the ESA.

Non-Enzymatic Detection of Glucose. The electrocatalytic properties of the CPNs were examined toward applications involving physiological pH such as the detection of Glu. Considering that Glu can be oxidized to gluconolactone at a neutral pH via a two-electron electrochemical reaction[64] and that the Co^{4+} ions may act as oxidizing species,[36] we propose that the prepared CPN material can catalyze the electrochemical oxidation of Glu (Figure 3a), which can be described by Equations 2 and 3:

$$2Co^{3+} \rightarrow 2Co^{4+} + 2e^{-} \quad (2)$$

$$2Co^{4+} + C_6H_{12}O_6\,(\text{glucose}) \rightarrow 2Co^{3+} + C_6H_{10}O_6\,(\text{gluconolactone}) + 2\,H+ \quad (3)$$

Therefore, electrooxidation of Glu on the CPNs for the non-enzymatic detection of Glu at physiological pH was investigated. Figure 3b compares the CVs of the CPN electrode and the bare GCE recorded in 0 and 30 mM Glu solutions (0, 10, 20, and 30 mM partially shown in inset) prepared in N_2-saturated PBS (10 mM, pH 7.4), as supporting electrolyte, at a scan rate of 20 mV/s in the potential region from –0.2 to 0.9 V, where the current density for this and all subsequent profiles are normalized by the ESA. The full CV profiles of the CPNs in various Glu solutions normalized by both the geometric area and the ESA of the electrode are shown in Figure S5. A noticeable Glu concentration-dependent increase of the anodic peak current was observed in the range of 0.3–0.8 V, which corresponds to the electrooxidation of Glu. The oxidation of Glu in PBS at pH 7.4 could be related to the formation of the electroactive Co^{4+} species. In contrast, the bare GCE (dashed line in Figure 3b) shows negligible current density and no apparent pair of redox peaks owing to the absence of electroactive species in the potential range from –0.2 to 0.9 V at all Glu solution concentrations studied.

To evaluate the concentration-dependent electrochemical response of the CPNs further, CA profiles in PBS electrolyte containing various amounts of Glu (Figure 3c) were recorded at an applied potential of 0.65 V. A step-like increase in current density upon addition of Glu at increasing concentrations was observed until a stable current density was achieved; 90% of the steady-state current density was achieved in 37 s (Figure S6). There was no current density drift observed after consecutively running the CA experiments thrice, using the same CPN-modified GCE for a total of 240 min (Figure S7), thus highlighting the stability and longevity

of the CPNs. Figure 3d shows the calibration curve that was constructed from the triplicate CA experiments. Interestingly, we notice an increase in the magnitude of the standard deviation in moving toward higher glucose concentrations, which may correspond to an increase in variability of detection as the CPNs approach the upper concentration limit of glucose.

The sensitivity of the CPN-modified GCE was 7.90 nA/mM cm^2 at a Glu concentration of 5 mM based on the ESA, and the LOD was 0.3 mM based on S/N = 3. Both the Glu detection range, tested up to 30 mM, and the LOD fulfill the requirements for Glu detection in human blood.[65] It is particularly interesting that the CPNs can catalyze the electrooxidation of Glu at physiological pH. In contrast, most of the existing cobalt-based catalysts that are used for non-enzymatic sensing of Glu require strong alkaline conditions.[23,39,41,42] Furthermore, while some other metal phosphate systems (e.g., $Ni_3(PO4)_2$-based materials[66]) have shown greater sensitivity for glucose detection than our currently reported materials, the detection range was investigated below the typical glucose concentration of human blood (i.e., <1 mM), and measurements were also performed in strongly alkaline conditions (1 M NaOH solutions).

Figure S8 shows the amperometric responsiveness of commercial $Co_3(PO_4)_2$ powder-based electrode for the electrooxidation of Glu. A similar trend was observed in terms of a step-like increase in current density as the Glu concentration is increased. Figure S9 shows the calibration curve that was constructed from the triplicate CA experiments. The powder displayed an LOD of 0.4 mM (S/N = 3) and a sensitivity of 4.53 nA/mM cm^2 at a Glu concentration of 5 mM based on the ESA, which is 43% lower compared than that of the CPNs. The results suggest that the CPN-improved sensitivity is due to the increased ESA as a result of the smaller dimensions and the spatial organization of the CPN building blocks when

compared with the $Co_3(PO_4)_2$ powder. The sensitivity and LOD were calculated, respectively, using Equations S2 and S3, and the fitting values are listed in Table S2.

Selectivity of CPNs in Physiological Contexts. For accurate Glu determination in biological contexts, it is important for the test material to exhibit selectivity toward Glu in the presence of other sugars and other oxidizable species in the human blood at their respective concentrations. Therefore, the selectivity of the CPNs toward Glu was studied in the presence of other sugars, such as lactose (LA) and galactose (GA), and other readily oxidizable species, such as ascorbic acid (AA) and dopamine (DP), at their physiological concentrations.[67-70] Figure 3e shows the CA profiles recorded at 0.65 V with successive additions of Glu (5 mM), LA (1.5 μM), GA (1.5 μM), AA (30 μM), DP (0.14 nM), and Glu (5 mM) to PBS (10 mM, pH 7.4) electrolyte under stirring. An increase in current density of about 50 nA/cm^2 was observed upon first addition of 5 mM Glu. In contrast, a significantly smaller increase in current (<10%) was observed upon subsequent addition of AA, and the increase in current was negligible following subsequent addition of LA, GA, and DP. The increase in current density (about 35 nA/cm^2) observed after the second addition of Glu shows that the CPNs are still responsive to Glu, and their activity is not compromised by the interfering agents. These results suggest that the CPNs are still capable of Glu sensing under the given experimental conditions. We do not suggest that the CPN material is only capable of sensing glucose, but instead suggest that it is capable of extrapolating

Moreover, the CPNs exhibit high tolerance against Cl^- poisoning considering that the experiments were conducted in PBS, which contains a high concentration of NaCl (137 mM).

It is known that chloride ions can poison non-enzymatic Glu sensors based on precious metals and alloys.[35,36,71]

Reusability of CPNs. The feasibility of reusing the same material (sensor) for multiple measurements is advantageous toward reducing costs and environmental impact. To demonstrate that the CPN-modified GCE can be reused multiple times, amperometric responses at 0.65 V were recorded in 0, 5, and 30 mM Glu PBS electrolyte; the electrode was washed with water after each measurement. Figure 3f shows that the current densities at the Glu concentrations studied were sustained across the multiple measurements performed, thus confirming that the CPN-modified GCE can effectively be reused after simple cleaning with water for reliable Glu sensing.

Thermostability of CPNs. To study the Glu sensing properties of the CPNs as a function of the electrolyte temperature, CA experiments were performed in triplicate as a function of temperature in 5 mM Glu PBS supporting electrolyte at a constant potential of 0.65 V. As observed in Figure S10, the current density was dependent on the temperature. The current density increased steadily with an increase in temperature up to 30 °C and increased more steeply with further increases in the temperature to 50 °C. From the electrochemical current densities at 30 and 50 °C, the calculated Glu concentrations (Table S2, fit 1) were respectively about 1 and 34 mM higher than the actual Glu concentration (5 mM). The concentration of Glu detected using the CPNs was consistent in the temperature range of 23–30 °C. Considering that, in general, the detection of Glu is performed within the temperature range of 23–30 °C, the CPNs are suitable for general use as a Glu sensor material. However, if a more precise

detection of Glu is needed, the effect of the temperature has to be taken into account, especially at temperatures higher than 30 °C.

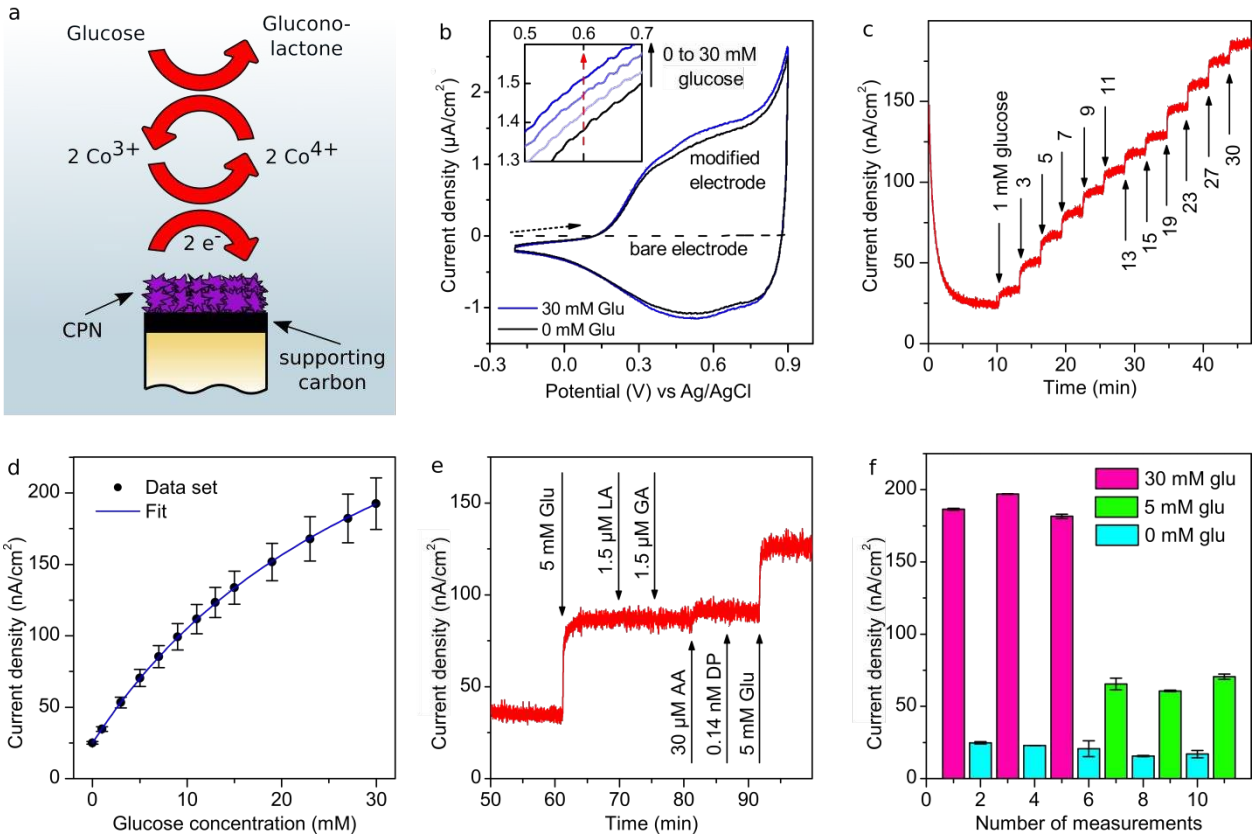

Figure 3. (a) Proposed electrochemical oxidation of Glu to gluconolactone at the electrode interface. (b) CVs of the CPN-modified electrode in PBS buffer (10 mM, pH 7.4) at a scan rate of 20 mV/s in the absence (black line) and presence (blue lines) of 30 mM Glu, respectively. The dashed line represents the CV of the GCE (bare electrode) obtained under the same experimental conditions. The inset shows a magnification of the potential region from 0.5 to 0.7 V (vs Ag/AgCl) with the presence of 10, 20, and 30 mM Glu (full profiles shown in Figure S5). (c) Chronoamperometric responses of the CPN in PBS buffer (10 mM, pH 7.4) to successive additions of Glu at an applied potential of 0.65 V (vs Ag/AgCl) and (d) the calibration curve

based on the triplicate CA experiments. (e) Amperometric responses of the CPNs at 0.65 V (vs Ag/AgCl) to the addition of Glu (5 mM) in PBS electrolyte (10 mM, pH 7.4), followed by additions of interfering agents lactose (LA, 1.5 μM), galactose (GA, 1.5 μM), ascorbic acid (AA, 30 μM), and dopamine (DP, 0.14 nM), and second addition of Glu (5 mM). (f) Cyclic amperometric responses of CPN-modified GCE in 0, 5, and 30 mM Glu; the CPN-modified GCE was washed with water after each measurement. Note that all current data have been normalized by the ESA and are not apparent current densities.

Calculations of the Interactions between the Cobalt Phosphate Surface and Glucose. We next investigated the mechanism of interaction between Glu and the CPN surface. To examine binding orientations of Glu on CPN surfaces, DFT calculations were performed. Relaxed surfaces of the (100), (111), and (211) facets of $Co_3(PO4)_2$ provided a variety of different possible cobalt coordination scenarios. The relaxed (100) surface presented cobalt in a 3-coordinate trigonal configuration, with a surface cobalt–cobalt distance of ~6 Å. The relaxed (111) and (211) surfaces presented cobalt in a variety of 3-, 4-, and 5-coordinate geometries, with surface cobalt–cobalt distances of 3–4 Å (Figure S11).

For the 3-coordinate Co arising from the relaxed (100) surface, the most energetically favorable binding of Glu was found to occur via the coordination of O1 to one Co atom at a distance of 2.10 Å and coordination of O3 to a second surface Co atom at a distance of 2.14 Å (Figure 4a). The binding energy of this configuration was calculated to be –1.42 eV (Table S3).

The most energetically favorable binding determined on the (111) surface was that between O1 and O2 of Glu and 3-coordinate cobalt, with oxygen–cobalt distances of 2.06 and 2.17 Å respectively (Figure 4b). The binding energy for this configuration was –1.52 eV. In contrast to the (100) surface, Glu binding on the (111) surface induced significant surface reconstruction upon binding, increasing the distance between the chelated cobalt and one of the phosphate oxygens from 2.06 to 2.31 Å.

Similar to the (111) surface, optimal Glu binding on the (211) surface was with a 3-coordinate cobalt adjacent to a 4-coordinate cobalt, and the O1 and O2 oxygens of Glu chelated the cobalt with oxygen–Glu distances of 2.02 and 2.04 Å, respectively (Figure 4c). However, the presence of an uncoordinated phosphate oxygen within 3 Å of the Glu O1 distinguishes the binding of Glu on the (211) surface from that observed on the (111) surface. It can be suggested that the electrooxidation of Glu is coupled to the proton transfer from the O1 hydroxyl group to the uncoordinated phosphate oxygen. Based on the calculations, this configuration exhibits the strongest binding with a binding energy of –1.86 eV. Glu binding configurations involving 4-coordinate and 5-coordinate cobalt on the (111) and (211) surfaces were generally less favorable, with binding energies of approximately –0.3 eV.

Though the results show an increase in binding strength with increasing facet index, it can be suggested that the key requirement for strong Glu binding and electrooxidation is the involvement of the distorted trigonal 3-coordinate geometry of cobalt on the surface, edge, or vertex where the O1 and O2 of Glu can chelate, regardless of the facet, neighboring uncoordinated phosphate oxygens. Interestingly, the most energetically favorable binding is

associated with maximizing the number of electrostatic contacts (e.g., coordinate bonds and hydrogen bonds), while minimizing the overall contact area (Table S3). Therefore, we suggest that the under-coordinated Co surface presentation scenarios associated with more highly faceted surfaces offers a greater distribution of electrostatic contacts, ultimately resulting in greater interactions with Glu.

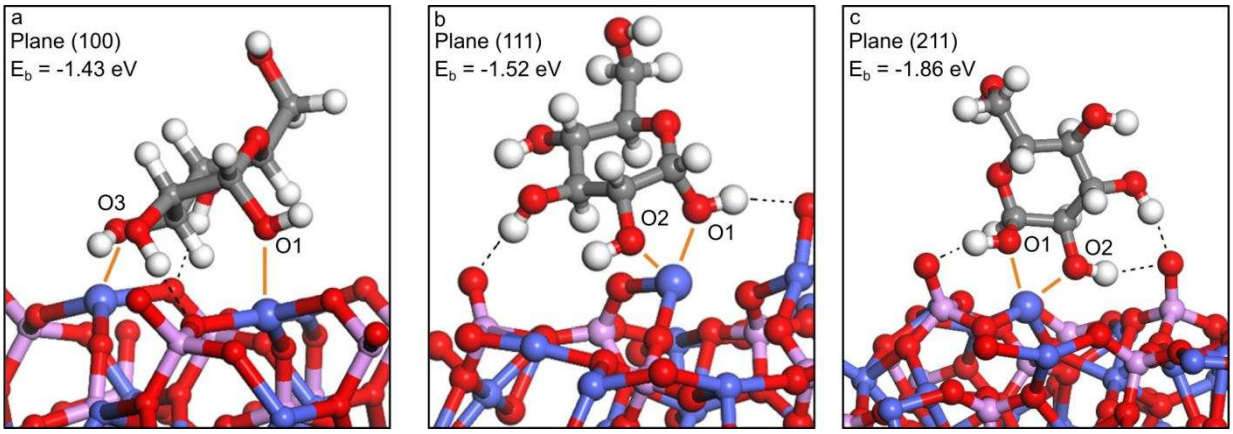

Figure 4. Energetically favorable Glu binding configurations and energies: (a) (100), (b) (111), and (c) (211) surfaces. Solid orange lines indicate coordination bonds and dotted black lines indicate hydrogen bonding. Cobalt, phosphorous, oxygen, carbon, and hydrogen are represented as blue, purple, red, grey, and white spheres, respectively.

Detection of Glucose in Human Serum. The ability of the CPNs to oxidize Glu suggests that they can be applied to biological samples such as HS. To examine the use of the CPNs for the detection of Glu in a complex matrix, such as HS, an SPE (Figure S12) with a drop-cast suspension of the CPNs was used. SPEs are suitable for the sensing of Glu owing to their miniaturized, portable, and disposable nature.[72] Figure 5a shows the calibration curves based

on the chronoamperometric responses of CPN-modified SPE upon addition of Glu in separate diluted solutions of HS, namely HS 1, 2, 5, 10% v/v in PBS, at an applied constant potential of 0.65 V (Figure S13). The error bars in Figure 5a represent the standard deviation of the steady-state current density at a given Glu concentration. The parameters of the fittings are shown in Table S2. The concentrations studied span up to 35 mM Glu, showing the broad detection range of the CPNs. Although, with an increase in the content of HS in PBS, a decrease in the CPN sensitivity and an increase in the LOD were observed, possibly owing to the fouling of biochemical species on the electrode surface (Figure S14). Nevertheless, the CPNs still show responsiveness toward the electrooxidation of Glu. Surface fouling from proteins, peptides, and lipids present in a biological matrix can inhibit electron transfers on an electrochemically active surface, causing a reduction in the analytical performances such as sensitivity, detection limit, and reproducibility.[73] This surface fouling causes deactivation of the electroactive sites, resulting in the decrease of electrocatalytic current relative to the oxidation of Glu. The stability of the CPNs in HS was also examined by recording 200 consecutive CV cycles in a 33 mM Glu HS 5% in PBS (Figure 5b). Throughout the 200 cycles, the CPNs showed no apparent decrease in current density at 0.65 V, as shown in the inset of Figure 5b, indicating its long service life and reliability. Future studies could focus on improving the system with various strategies in order to minimize protein, peptide, and lipid fouling. Such strategies could involve the surface coverage of the electrode with antifouling materials, such as polyvinylpyrrolidone or polyethylene glycol, or pre-filtering the HS to remove the fouling substances.

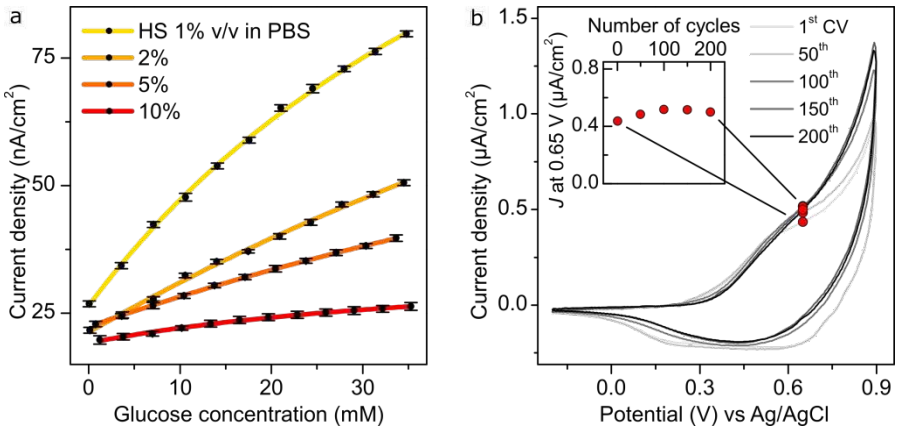

Figure 5. (a) Calibration curves with the relative fittings based on the chronoamperometric response of the CPN-modified SPE in the electrolyte composed of HS diluted with PBS (10 mM, pH 7.4) to the successive addition of Glu at an applied potential of 0.65 V (vs Ag/AgCl) (the raw data prior to fitting are shown in Figure S13). (b) Consecutive CVs of the CPNs in a 33 mM Glu HS 5% v/v in PBS electrolyte after activation. The inset shows the changes in the current density at 0.65 V (vs Ag/AgCl) as the cycle number is increased from 1 to 200. All current density data are normalized by the ESA.

CONCLUSIONS

We reported the synthesis of electrocatalytically active CPNs using a simple, low-cost, and scalable crystallization method. We investigated the electrocatalytic properties of the CPNs for non-enzymatic Glu detection—rod- and screen-printed electrodes were modified with CPNs for the catalyzed oxidation of Glu in a relevant biological environment such as PBS electrolyte at physiological pH of 7.4. The CPNs achieved a wide Glu detection range (from 1 to 30 mM Glu in PBS) with a sensitivity of 7.90 nA/mM cm^2 at 5 mM of Glu (based on the electroactive surface area of the electrode) and a limit of detection of 0.3 mM. The CPN system

was stable—no drifts in the current density were observed during the determination of Glu in both PBS and diluted solutions of HS, thus suggesting the longevity and reliability of the CPN system. Additionally, the CPNs displayed negligible catalytic activity toward the oxidation of coexisting interfering species such as lactose, galactose, ascorbic acid, and dopamine, thus demonstrating the specificity of the CPN system toward Glu detection. The CPNs were applied in biologically relevant electrolytes, such as diluted solutions of HS in PBS, where the CPNs achieved a wide detection range up to 35 mM Glu, with a sensitivity depending on the concentration of HS. DFT calculations suggested that the optimal binding of Glu occurred at under-coordinated cobalt atoms at the surface, edge, or vertex of the nanostructure. Our results suggest the potential application of the CPN-modified electrodes for the non-enzymatic detection of Glu under biological conditions.

ASSOCIATED CONTENT

Supporting information. EDX data, XPS survey, CV and CA experiments, photograph of SPE, fitting data, and DFT simulations.

AUTHOR INFORMATION

Corresponding Authors

*Email: fcaruso@unimelb.edu.au.

*Email: francesca.cavalieri@unimelb.edu.au.

Present Address

⊥Centre for Advanced 2D Materials, National University of Singapore, Singapore.

Author Contributions

All authors have given approval to the final version of the manuscript.

Funding Sources

This work was supported by the Australian Research Council (ARC) under a Future Fellowship (F. Cavalieri, FT140100873) and a National Health and Medical Research Council Fellowship (F. Caruso, APP1135806). This research was conducted and supported by the ARC Centre of Excellence in Convergent Bio-Nano Science and Technology (project number CE140100036). This work was also supported by a University of Melbourne Establishment Grant (F. Cavalieri).

Notes

The authors declare no competing financial interest.

ACKNOWLEDGMENT

This work was performed in part at the Materials Characterisation and Fabrication Platform (MCFP) at The University of Melbourne and the Victorian Node of the Australian National Fabrication Facility (ANFF). Transmission electron microscopy was undertaken at the Biosciences Microscopy Unit, School of Biosciences, The University of Melbourne. We thank Roger Curtain from the Bio21 Advanced Microscopy Facility (The University of Melbourne) for assistance with SEM and Prof. Francesco Ricci (University of Rome, Tor Vergata) for kindly

providing the SPE. This research was undertaken with the assistance of resources and services from the National Computational Infrastructure (NCI), which is supported by the Australian Government.

References

(1) Zhou, Z.-Y.; Tian, N.; Li, J.-T.; Broadwell, I.; Sun, S.-G. Nanomaterials of High Surface Energy with Exceptional Properties in Catalysis and Energy Storage. *Chem. Soc. Rev.* **2011**, *40*, 4167–4185.
(2) Martinez, C. J.; Hockey, B.; Montgomery, C. B.; Semancik, S. Porous Tin Oxide Nanostructured Microspheres for Sensor Applications. *Langmuir* **2005**, *21*, 7937–7944.
(3) Zhang, Y.-Z.; Wang, Y.; Cheng, T.; Lai, W.-Y.; Pang, H.; Huang, W. Flexible Supercapacitors Based on Paper Substrates: A New Paradigm for Low-Cost Energy Storage. *Chem. Soc. Rev.* **2015**, *44*, 5181–5199.
(4) Awazu, K.; Fujimaki, M.; Rockstuhl, C.; Tominaga, J.; Murakami, H.; Ohki, Y.; Yoshida, N.; Watanabe, T. Plasmonic Photocatalyst Consisting of Silver Nanoparticles Embedded in Titanium Dioxide. *J. Am. Chem. Soc.* **2008**, *130*, 1676–1680.
(5) Chan, C. K.; Peng, H.; Liu, G.; McIlwrath, K.; Zhang, X. F.; Huggins, R. A.; Cui, Y. High-Performance Lithium Battery Anodes Using Silicon Nanowires. *Nat. Nanotechnol.* **2008**, *3*, 31–35.
(6) Voiry, D.; Yamaguchi, H.; Li, J.; Silva, R.; Alves, D. C. B.; Fujita, T.; Chen, M.; Asefa, T.; Shenoy, V. B.; Eda, G. Enhanced Catalytic Activity in Strained Chemically Exfoliated WS_2 Nanosheets for Hydrogen Evolution. *Nat. Mater.* **2013**, *12*, 850–855.
(7) Chen, A.; Peng, X.; Koczkur, K.; Miller, B. Super-Hydrophobic Tin Oxide Nanoflowers. *Chem. Commun.* **2004**, 1964–1965.
(8) Ge, J.; Lei, J.; Zare, R. N. Protein–Inorganic Hybrid Nanoflowers. *Nat. Nanotechnol.* **2012**, *7*, 428–432.
(9) Zhang, Z.; Zhang, Y.; Song, R.; Wang, M.; Yan, F.; He, L.; Feng, X.; Fang, S.; Zhao, J.; Zhang, H. Manganese(II) Phosphate Nanoflowers as Electrochemical Biosensors for the High-Sensitivity Detection of Ractopamine. *Sens. Actuators, B* **2015**, *211*, 310–317.
(10) Wang, L.-B.; Wang, Y.-C.; He, R.; Zhuang, A.; Wang, X.; Zeng, J.; Hou, J. G. A New Nanobiocatalytic System Based on Allosteric Effect with Dramatically Enhanced Enzymatic Performance. *J. Am. Chem. Soc* **2013**, *135*, 1272–1275.
(11) Kim, K. H.; Jeong, J.-M.; Lee, S. J.; Choi, B. G.; Lee, K. G. Protein-Directed Assembly of Cobalt Phosphate Hybrid Nanoflowers. *J. Colloid Interface Sci.* **2016**, *484*, 44–50.
(12) Luo, Y.-K.; Song, F.; Wang, X.-L.; Wang, Y.-Z. Pure Copper Phosphate Nanostructures with Controlled Growth: A Versatile Support for Enzyme Immobilization. *CrystEngComm* **2017**, *19*, 2996–3002.
(13) Theerthagiri, J.; Thiagarajan, K.; Senthilkumar, B.; Khan, Z.; Senthil, R. A.; Arunachalam, P.; Madhavan, J.; Ashokkumar, M. Synthesis of Hierarchical Cobalt Phosphate Nanoflakes and Their Enhanced Electrochemical Performances for Supercapacitor Applications. *ChemistrySelect* **2017**, *2*, 201–210.

(14) Chen, C.; Kang, Y.; Huo, Z.; Zhu, Z.; Huang, W.; Xin, H. L.; Snyder, J. D.; Li, D.; Herron, J. A.; Mavrikakis, M. Highly Crystalline Multimetallic Nanoframes with Three-Dimensional Electrocatalytic Surfaces. *Science* **2014**, *343*, 1339–1343.
(15) Klinkova, A.; Cherepanov, P. V.; Ryabinkin, I. G.; Ho, M.; Ashokkumar, M.; Izmaylov, A. F.; Andreeva, D. V.; Kumacheva, E. Shape-Dependent Interactions of Palladium Nanocrystals with Hydrogen. *Small* **2016**, *12*, 2450–2458.
(16) Klinkova, A.; De Luna, P.; Sargent, E. H.; Kumacheva, E.; Cherepanov, P. V. Enhanced Electrocatalytic Performance of Palladium Nanoparticles with High Energy Surfaces in Formic Acid Oxidation. *J. Mater. Chem. A* **2017**, *5*, 11582–11585.
(17) Popczun, E. J.; Roske, C. W.; Read, C. G.; Crompton, J. C.; McEnaney, J. M.; Callejas, J. F.; Lewis, N. S.; Schaak, R. E. Highly Branched Cobalt Phosphide Nanostructures for Hydrogen-Evolution Electrocatalysis. *J. Mater. Chem. A* **2015**, *3*, 5420–5425.
(18) Dong, X.-C.; Xu, H.; Wang, X.-W.; Huang, Y.-X.; Chan-Park, M. B.; Zhang, H.; Wang, L.-H.; Huang, W.; Chen, P. 3D Graphene–Cobalt Oxide Electrode for High-Performance Supercapacitor and Enzymeless Glucose Detection. *ACS Nano* **2012**, *6*, 3206–3213.
(19) Ji, X.; Zhang, R.; Shi, X.; Asiri, A. M.; Zheng, B.; Sun, X. Fabrication of Hierarchical CoP Nanosheet@Microwire Arrays via Space-Confined Phosphidation toward High-Efficiency Water Oxidation Electrocatalysis under Alkaline Conditions. *Nanoscale* **2018**, *10*, 7941–7945.
(20) Tian, J.; Cheng, N.; Liu, Q.; Xing, W.; Sun, X. Cobalt Phosphide Nanowires: Efficient Nanostructures for Fluorescence Sensing of Biomolecules and Photocatalytic Evolution of Dihydrogen from Water under Visible Light. *Angew. Chem., Int. Ed.* **2015**, *54*, 5493–5497.
(21) Xie, F.; Liu, T.; Xie, L.; Sun, X.; Luo, Y. Metallic Nickel Nitride Nanosheet: An Efficient Catalyst Electrode for Sensitive and Selective Non-Enzymatic Glucose Sensing. *Sens. Actuators, B* **2018**, *255*, 2794–2799.
(22) Liu, T.; Xie, L.; Yang, J.; Kong, R.; Du, G.; Asiri, A. M.; Sun, X.; Chen, L. Self-Standing CoP Nanosheets Array: A Three-Dimensional Bifunctional Catalyst Electrode for Overall Water Splitting in Both Neutral and Alkaline Media. *ChemElectroChem* **2017**, *4*, 1840–1845.
(23) Han, L.; Yang, D.-P.; Liu, A. Leaf-Templated Synthesis of 3D Hierarchical Porous Cobalt Oxide Nanostructure as Direct Electrochemical Biosensing Interface with Enhanced Electrocatalysis. *Biosens. Bioelectron.* **2015**, *63*, 145–152.
(24) Ferri, S.; Kojima, K.; Sode, K., Review of Glucose Oxidases and Glucose Dehydrogenases: A Bird's Eye View of Glucose Sensing Enzymes. *J. Diabetes Sci. Technol.* **2011**, *5*, 1068–1076.
(25) Sun, J.; Ge, J.; Liu, W.; Lan, M.; Zhang, H.; Wang, P.; Wang, Y.; Niu, Z. Multi-Enzyme Co-Embedded Organic–Inorganic Hybrid Nanoflowers: Synthesis and Application as a Colorimetric Sensor. *Nanoscale* **2014**, *6*, 255–262.
(26) Santana-Jiménez, L. A.; Márquez-Lucero, A.; Osuna, V.; Estrada-Moreno, I.; Dominguez, R. B. Naked-Eye Detection of Glucose in Saliva with Bienzymatic Paper-Based Sensor. *Sensors* **2018**, *18*, 1071.
(27) Russell, R. J.; Pishko, M. V.; Gefrides, C. C.; McShane, M. J.; Cote, G. L. A Fluorescence-Based Glucose Biosensor Using Concanavalin A and Dextran Encapsulated in a Poly(ethylene glycol) Hydrogel. *Anal. Chem.* **1999**, *71*, 3126–3132.

(28) Sun, X.; James, T. D. Glucose Sensing in Supramolecular Chemistry. *Chem. Rev.* **2015**, *115*, 8001–8037.
(29) Chen, X.; Tian, X.; Zhao, L.; Huang, Z.; Oyama, M. Nonenzymatic Sensing of Glucose at Neutral pH Values Using a Glassy Carbon Electrode Modified with Graphene Nanosheets and Pt-Pd Bimetallic Nanocubes. *Microchim. Acta* **2014**, *181*, 783–789.
(30) Mei, H.; Wu, W.; Yu, B.; Li, Y.; Wu, H.; Wang, S.; Xia, Q. Non-Enzymatic Sensing of Glucose at Neutral pH Values Using a Glassy Carbon Electrode Modified with Carbon Supported Co@Pt Core-Shell Nanoparticles. *Microchim. Acta* **2015**, *182*, 1869–1875.
(31) Koschinsky, T.; Heinemann, L. Sensors for Glucose Monitoring: Technical and Clinical Aspect. *Diabetes/Metab. Res. Rev.* **2001**, *17*, 113–123.
(32) Wilson, R.; Turner, A. P. F. Glucose Oxidase: An Ideal Enzyme. *Biosens. Bioelectron.* **1992**, *7*, 165–185.
(33) Yuan, J. H.; Wang, K.; Xia, X. H. Highly Ordered Platinum-Nanotubule Arrays for Amperometric Glucose Sensing. *Adv. Funct. Mater.* **2005**, *15*, 803–809.
(34) Soomro, R. A.; Akyuz, O. P.; Ozturk, R.; Ibupoto, Z. H. Highly Sensitive Non-Enzymatic Glucose Sensing Using Gold Nanocages as Efficient Electrode Material. *Sens. Actuators, B* **2016**, *233*, 230–236.
(35) Sun, Y.; Buck, H.; Mallouk, T. E. Combinatorial Discovery of Alloy Electrocatalysts for Amperometric Glucose Sensors. *Anal. Chem.* **2001**, *73*, 1599–1604.
(36) Ding, Y.; Wang, Y.; Su, L.; Bellagamba, M.; Zhang, H.; Lei, Y. Electrospun Co_3O_4 Nanofibers for Sensitive and Selective Glucose Detection. *Biosens. Bioelectron.* **2010**, *26*, 542–548.
(37) Premlatha, S.; Sivasakthi, P.; Bapu, G. N. K. R. Electrodeposition of a 3D Hierarchical Porous Flower-Like Cobalt–MWCNT Nanocomposite Electrode for Non-Enzymatic Glucose Sensing. *RSC Adv.* **2015**, *5*, 74374–74380.
(38) Jiang, D.; Liu, Q.; Wang, K.; Qian, J.; Dong, X.; Yang, Z.; Du, X.; Qiu, B. Enhanced Non-Enzymatic Glucose Sensing Based on Copper Nanoparticles Decorated Nitrogen-Doped Graphene. *Biosens. Bioelectron.* **2014**, *54*, 273–278.
(39) Huang, B.; Wang, Y.; Lu, Z.; Du, H.; Ye, J. One Pot Synthesis of Palladium-Cobalt Nanoparticles over Carbon Nanotubes as a Sensitive Non-Enzymatic Sensor for Glucose and Hydrogen Peroxide Detection. *Sens. Actuators, B* **2017**, *252*, 1016–1025.
(40) Kang, L.; He, D.; Bie, L.; Jiang, P. Nanoporous Cobalt Oxide Nanowires for Non-Enzymatic Electrochemical Glucose Detection. *Sens. Actuators, B* **2015**, *220*, 888–894.
(41) Chung, J. S.; Hur, S. H. A Highly Sensitive Enzyme-Free Glucose Sensor Based on Co_3O_4 Nanoflowers and 3D Graphene Oxide Hydrogel Fabricated via Hydrothermal Synthesis. *Sens. Actuators, B* **2016**, *223*, 76–82.
(42) Liu, T.; Li, M.; Dong, P.; Zhang, Y.; Guo, L. Design and Facile Synthesis of Mesoporous Cobalt Nitride Nanosheets Modified by Pyrolytic Carbon for the Nonenzymatic Glucose Detection. *Sens. Actuators, B* **2018**, *255*, 1983–1994.

(43) Soomro, R. A.; Ibupoto, Z. H.; Abro, M. I.; Willander, M. Electrochemical Sensing of Glucose Based on Novel Hedgehog-Like NiO Nanostructures. *Sens. Actuators, B* **2015**, *209*, 966–974.
(44) Anderson, J. B.; Kostiner, E.; Miller, M. C.; Rea, J. R. The Crystal Structure of Cobalt Orthophosphate $Co_3(PO_4)_2$. *J. Solid State Chem.* **1975**, *14*, 372–377.
(45) Kresse, G.; Furthmüller, J. Efficient Iterative Schemes for Ab Initio Total-Energy Calculations Using a Plane-Wave Basis Set. *Phys. Rev. B* **1996**, *54*, 11169.
(46) Perdew, J. P.; Burke, K.; Ernzerhof, M. Generalized Gradient Approximation Made Simple. *Phys. Rev. Lett.* **1996**, *77*, 3865.
(47) Kresse, G.; Joubert, D. From Ultrasoft Pseudopotentials to the Projector Augmented-Wave Method. *Phys. Rev. B* **1999**, *59*, 1758.
(48) Blöchl, P. E. Projector Augmented-Wave Method. *Phys. Rev. B* **1994**, *50*, 17953.
(49) Monkhorst, H. J.; Pack, J. D. Special Points for Brillouin-Zone Integrations. *Phys. Rev. B* **1976**, *13*, 5188.
(50) Wang, L.; Maxisch, T.; Ceder, G. Oxidation Energies of Transition Metal Oxides within the GGA+U Framework. *Phys. Rev. B* **2006**, *73*, 195107.
(51) Kim, H.; Park, J.; Park, I.; Jin, K.; Jerng, S. E.; Kim, S. H.; Nam, K. T.; Kang, K. Coordination Tuning of Cobalt Phosphates towards Efficient Water Oxidation Catalyst. *Nat. Commun.* **2015**, *6*, 8253.
(52) Cabrera-German, D.; Gomez-Sosa, G.; Herrera-Gomez, A. Accurate Peak Fitting and Subsequent Quantitative Composition Analysis of the Spectrum of Co 2p Obtained with Al Kα Radiation: I: Cobalt Spinel. *Surf. Interface Anal.* **2016**, *48*, 252–256.
(53) Biesinger, M. C.; Payne, B. P.; Grosvenor, A. P.; Lau, L. W. M.; Gerson, A. R.; Smart, R. S. C. Resolving Surface Chemical States in XPS Analysis of First Row Transition Metals, Oxides and Hydroxides: Cr, Mn, Fe, Co and Ni. *Appl. Surf. Sci.* **2011**, *257*, 2717–2730.
(54) Sun, Q.-Q.; Wang, M.; Bao, S.-J.; Wang, Y. C.; Gu, S. Analysis of Cobalt Phosphide (CoP) Nanorods Designed for Non-Enzyme Glucose Detection. *Analyst* **2016**, *141*, 256–260.
(55) Dzyuba, E. D.; Shchegrov, L. N.; Pechkovskii, V. V.; Mel'Nikova, R. Y. Infrared Absorption Spectra of Disubstituted Cobalt Phosphate. *J. Appl. Spectrosc.* **1970**, *12*, 666–669.
(56) Corbridge, D. E. C.; Lowe, E. J. The Infra-Red Spectra of Inorganic Phosphorus Compounds. Part II. Some Salts of Phosphorus Oxy-Acids. *J. Am. Chem. Soc.* **1954**, 4555–4564.
(57) Tang, C.-W.; Wang, C.-B.; Chien, S.-H. Characterization of Cobalt Oxides Studied by FT-IR, Raman, TPR and TG-MS. *Thermochim. Acta* **2008**, *473*, 68–73.
(58) Acerce, M.; Voiry, D.; Chhowalla, M. Metallic 1T Phase MoS_2 Nanosheets as Supercapacitor Electrode Materials. *Nat. Nanotechnol.* **2015**, *10*, 313.
(59) Kannan, P.; Maiyalagan, T.; Marsili, E.; Ghosh, S.; Niedziolka-Jönsson, J.; Jönsson-Niedziolka, M. Hierarchical 3-Dimensional Nickel–Iron Nanosheet Arrays on Carbon Fiber Paper as a Novel Electrode for Non-Enzymatic Glucose Sensing. *Nanoscale* **2016**, *8*, 843–855.

(60) Goyal, R. N.; Gupta, V. K.; Chatterjee, S. Voltammetric Biosensors for the Determination of Paracetamol at Carbon Nanotube Modified Pyrolytic Graphite Electrode. *Sens. Actuators, B* **2010**, *149*, 252–258.
(61) Konopka, S. J.; McDuffie, B. Diffusion Coefficients of Ferri- and Ferrocyanide Ions in Aqueous Media, Using Twin-Electrode Thin-Layer Electrochemistry. *Anal. Chem.* **1970**, *42*, 1741–1746.
(62) Yu, H.; Jin, J.; Jian, X.; Wang, Y.; Qi, G. c. Preparation of Cobalt Oxide Nanoclusters/Overoxidized Polypyrrole Composite Film Modified Electrode and Its Application in Nonenzymatic Glucose Sensing. *Electroanalysis* **2013**, *25*, 1665–1674.
(63) Casella, I. G.; Gatta, M. Study of the Electrochemical Deposition and Properties of Cobalt Oxide Species in Citrate Alkaline Solutions. *J. Electroanal. Chem.* **2002**, *534*, 31–38.
(64) Tominaga, M.; Shimazoe, T.; Nagashima, M.; Taniguchi, I. Electrocatalytic Oxidation of Glucose at Gold Nanoparticle-Modified Carbon Electrodes in Alkaline and Neutral Solutions. *Electrochem. Commun.* **2005**, *7*, 189–193.
(65) Bruen, D.; Delaney, C.; Florea, L.; Diamond, D. Glucose Sensing for Diabetes Monitoring: Recent Developments. *Sensors* **2017**, *17*, 1866.
(66) Padmanathan, N.; Shao, H.; Razeeb, K.M. Multifunctional Nickel Phosphate Nano/Microflakes 3D Electrode for Electrochemical Energy Storage, Nonenzymatic Glucose, and Sweat pH Sensors. *ACS Appl. Mater. Interfaces* **2018**, 10, 8599-8610.
(67) Arthur, P. G.; Kent, J. C.; Potter, J. M.; Hartmann, P. E. Lactose in Blood in Nonpregnant, Pregnant, and Lactating Women. *J. Pediatr. Gastroenterol. Nutr.* **1991**, *13*, 254–259.
(68) Schadewaldt, P.; Hammen, H.-W.; Loganathan, K.; Bodner-Leidecker, A.; Wendel, U. Analysis of Concentration and ^{13}C enrichment of D-Galactose in Human Plasma. *Clin. Chem.* **2000**, *46*, 612–619.
(69) Sargent, F. Study of the Normal Distribution of Ascorbic Acid between the Red Cells and Plasma of Human Blood. *J. Biol. Chem.* **1947**, *171*, 471–476.
(70) Ambade, V.; Brig, M. M. A.; Col, P. S. R.; Somani, B. L.; Basannar, D. Adrenaline, Noradrenaline and Dopamine Level Estimation in Depression: Does It Help? *Med. J. Armed Force India* **2009**, *65*, 216–220.
(71) Park, S.; Chung, T. D.; Kim, H. C. Nonenzymatic Glucose Detection Using Mesoporous Platinum. *Anal. Chem.* **2003**, *75*, 3046–3049.
(72) Choudhry, N. A.; Kampouris, D. K.; Kadara, R. O.; Jenkinson, N.; Banks, C. E. Next Generation Screen Printed Electrochemical Platforms: Non-Enzymatic Sensing of Carbohydrates Using Copper(II) Oxide Screen Printed Electrodes. *Anal. Methods* **2009**, *1*, 183–187.
(73) Hanssen, B. L.; Siraj, S.; Wong, D. K. Y. Recent Strategies to Minimise Fouling in Electrochemical Detection Systems. *Rev. Anal. Chem* **2016**, *35*, 1–28.

Table of Content Graphic